Zonal and Regional Jupiter Brightness Trends from the Hubble Outer Planet Atmospheres Legacy Program

Amy A. Simon[1] and Michael H. Wong[2]

Abstract

The Hubble Outer Planet Atmospheres Legacy (OPAL) program began in 2014 and has observed Jupiter yearly from 2015 to 2024. Using high spatial resolution imaging from the Hubble Wide Field Camera 3, brightness trends were investigated focusing on the unique UV capability and absolute calibration consistency of the Hubble Space Telescope. From these data, a 4- to 5- year period is observed at 24° N, particularly in the blue (F395N) and methane gas absorption (FQ889N) filters. Additionally, several wavelengths show a potential seasonal periodicity, especially at the equator, but more years of data are needed to confirm this trend over multiple Jupiter years. Variability in Oval BA and the Great Red Spot brightness is not cyclical, but these two anticyclonic features show changes on a yearly timescale.

[1] NASA Goddard Space Flight Center, Code 690, Greenbelt, MD 20771, USA. Corresponding author email: amy.simon@nasa.gov
[2] University of California Berkeley, Space Sciences Laboratory, Berkeley, CA 94720, USA

1. Introduction

Changes in Jupiter's colored belts and white zones have long fascinated observers (Peek 1958, Rogers 1995). Historical observers often recorded major changes in the color of Jupiter's largest bands, particularly the Equatorial Zone (EZ) and the North and South Equatorial Belts (NEB and SEB, respectively), sometimes in a sequence of color changes from band to band in a few-year period, subsequently labeled as a global upheaval (Wacker 1975, Rogers 1995), though it is unknown what drives these changes. It should be noted that in the oldest records, Jupiter's typical colors were used to define the latitudes of the belts (usually dark) and zones (usually bright), and thus their edges could vary; we now use the zonal wind pattern to define the belt/zone edges, regardless of their coloration (e.g., Beebe 1994). Although the historical record spans more than 150 years, colors and features were often described in fanciful terms, and inconsistencies in collection methods make those data impossible to analyze in terms of absolute color (Peek 1958, Rogers 1995).

From the historical records, major cycles of coloration were identified, but they did not always occur at regular intervals and the causes were not understood (Wacker 1975, Rogers 1995). For example, the EZ (7° N to 7° S planetographic latitude) went from bright to darker every 2 to 5 years in the 1920s to 1970s, changed on a seasonal (~12 year) cycle in the 1980 to 1990 period, then remained bright for over a full Jovian year in the 1990s (Rogers 1995). However, the reports are based on visual interpretations of coloration, while the absolute intensity can be quite variable.

The NEB (~7° to 17° N) and SEB (~7° to 20° S) are more complex to interpret in the historical record. Observations in the 1800s indicated that both changed coloration on an ~11-year period, but later observations were not as conclusive (Peek 1958). We now know these regions can be influenced by convective activity, waves, and vortices that cause these belts to "fade" whiter, undergo a convective "revival" to a darker state, and sometimes even "expand" outside their normal latitude bands and into the North or South Tropical Zones (Rogers 1995, Fletcher et al. 2017a, 2017b). Cycles of activity, particularly the fade/revival stages, can occur on a 3 to 5-year period, but sometimes the period is

longer, effectively skipping a cycle. In the late 1800s to early 1900s, the expansion phase of the NEB into the NTrZ tended to occur a bit more rarely (Rogers 1995), but a further analysis of ground-based data from 1987 to 2024 indicates a clear 3 to 5-year period for NEB expansions (Rogers et al. 2017, Fletcher 2017, Rogers 2019).

The most recurrent color change in the historical record occurs a bit farther north, in the North Temperate Belt, with coloration events every 10 years (Rogers 1995). Starting in the 1970s, approximately every 5 years bright plumes of activity were also noted, along with increased cloud speeds on the 24° N wind jet (Rogers 1995). Starting in 2012, the convective outbreaks occurred every 4 years (Fletcher 2017, Sánchez-Lavega et al. 2017, Rogers & Adamoli 2019).

Modern telescopic and spacecraft observations have also added to the long record of Jupiter activity, and with expanded wavelength coverage into the ultraviolet and infrared (Simon et al. 2022). In this era, an approximately 4-year cycle was found primarily in stratospheric IR brightness temperatures and dubbed the quasi-quadrennial oscillation (QQO) (Orton et al. 1991, Leovy et al. 1991). This oscillation is thought to be similar to stratospheric oscillations on Earth, driven by vertically propagating low latitude waves (Leovy et al. 1991, Baldwin et al. 2001). After the driving waves break in the stratosphere, there is a descending temperature pattern that could drive tropospheric cloud and wind variations (Leovy et al. 1991). However, more recent IR data show that the QQO period is variable, between 3.9 and 5.7-years, and sometimes disrupted by major planetary-scale disturbances at these latitudes (Antuñano et al. 2021).

Prior Hubble studies (Simon-Miller et al. 2007, Simon-Miller & Gierasch 2010) searched for low latitude trends in brightness and winds that might be tied to the QQO or other cycles. While the brightness variations in ~15 years of Wide Field Planetary Camera 2 (WFPC2) data showed hints of interesting periodicities near the equator, the results were inconclusive due to uncertainties from long-term drift in WFPC2 detector sensitivity and calibration, particularly at UV wavelengths (McMaster & Whitmore 2002, Gonzaga et al., 2006, McMaster & Biretta 2008), as well as gaps in data coverage.

To better understand the underlying causes of Jovian activity requires regular high spatial-resolution, broad wavelength, absolutely calibrated, data to identify trends in cloud-level color and convective activity. The Hubble Outer Planet Atmospheres Legacy (OPAL) program was introduced to provide absolutely calibrated UV to IR data for temporal studies of the outer planets. Using the Wide Field Camera 3 (WFC3) UVIS channel, OPAL observes each planet over two full planetary rotations each year, allowing complete 2D wind mapping, as well as trending in cloud brightness and color, and tracking of long-term storms (Simon et al. 2015b). Due to guide star lock failures or gyro issues, there are sometimes gaps that preclude two complete maps, but there is at least one full rotation captured every year, and maps are posted to the Hubble High Level Science Product archive (https://archive.stsci.edu/hlsp/opal). The OPAL filters for Jupiter were selected to give consistent trending of cloud color as well as altitude, using a range of continuum filters from 275 to 631 nm and the 889-nm methane gas absorption band. OPAL began observing Jupiter with Hubble WFC3 in 2015, and ten years of coverage have now been obtained.

The OPAL Jupiter data have already been mined in several wind velocity trending studies. Using both older and OPAL Hubble data, new zonal wind profiles were obtained over many years using a variety of correlation techniques to search for spatial or temporal variations (Tollefson et al 2017, Johnson et al. 2018). It was found that there is little longitudinal variation in the zonal winds, except for the location of the Great Red Spot (GRS) (Johnson et al. 2018). In temporal space, the zonal winds do not match cloud top changes, as the jets are largely stable over time and most “changes” can be attributed to measurement technique and which cloud features are measured (e.g., large waves at 7° N and S cause difficulty in defining the underlying wind field, as described in Legaretta et al. (2016) and references therein). Caution is especially warranted in interpreting wind profiles from lower resolution data where the smallest cloud features may not be resolved, and in those measured with older correlation techniques which often missed the peak jet velocities. A notable exception occurs in the highest velocity wind jet at 24°N latitude, which does noticeably change velocity during outbreaks of activity (Rogers 1995, Sánchez-Lavega et al. 2008, Asay-Davis et al. 2011, Sánchez-Lavega et al. 2017). A smaller storm

outbreak series in the SEB (de Pater et al. 2019) also led to a limited change of about 20 m/s in wind speeds between 10° S and 15° S (Wong et al. 2020). Even with the higher resolution data and consistently mapped wind profiles, there are few periodicities of any particular wind jet, other than possibly at the equator (Tollefson et al. 2017).

A major remaining goal of the OPAL program is to trend changes in cloud color and brightness across the four giant planets, as these changes tie to cloud structure and the unknown deeper circulation. Fry and Sromovsky (2023) previously reported on brightness data and cloud structure from 2015 to 2020. In this work, we expand the OPAL coverage with Jupiter data for ~10 years, supplemented with WFC3 data from earlier programs to extend the temporal coverage to a full Jupiter year, even though full longitudinal coverage was not typically available. In this manuscript we focus on and analyze Jupiter's zonal brightness changes and correlate them with possible seasonal or short-period cycles, as well report brightness trends in two large anticyclonic vortices, Oval BA and the GRS. Section 2 describes the data we selected and the processing. Section 3 describes the analysis of zonal changes. Section 4 looks at longitudinal variations. Sections 5 and 6 analyze the GRS and Oval BA, respectively. Lastly, we discuss our results in the context of known cycles.

2. Data Sets and Image Processing

Installed in 2009, the Wide Field Camera 3 (WFC3) has improved spatial resolution over its predecessors and consistent photometric monitoring (Marinelli and Dressel 2024). The WFC3 photometry has been much more stable than that from WFPC2 (which suffered from temporal UV contamination issues, CTE loss), as well as a better characterized FQ889N filter (WFPC2 suffered from severe vignetting and blue leaks) (Karkoschka and Koekemoer 2003, McMaster et al. 2008). Although WFC3 also has some time-variable sensitivity, this is now better accounted for in the calibration pipeline (Marinelli and Dressel 2024). The narrowband long wavelength filters, particularly FQ889N, suffer from optical etaloning, but this can be reduced in post-pipeline defringing (Wong 2011) – this correction is applied to all images in the OPAL maps, but was not applied in individual images for this

study (it represents a few percent effect in the photometric accuracy (Wong 2010)). The absolute calibration uncertainties are on the order of a few percent for most filters and ~5% for the FQ889N filter, with relative uncertainties (precision) better than 1% (Marinelli and Dressel 2024).

We searched the MAST archive for Jupiter WFC3 images across all available dates, as well as the coverage from OPAL. We chose WFC3 UVIS filters that serve as a proxy for high altitude clouds (FQ889N) and hazes (F275W), cloud color (F395N), and vertically integrated cloud deck opacity (F631N). Images were chosen to allow quasi-yearly coverage, when possible, Table 1. In some years there are additional data sets, but we chose the sets that best spanned the time coverage rather than having several very close (within a few months of each other) in time. After selecting images that gave the best temporal coverage, we retrieved the latest pipeline calibrated images for analysis and all images were processed identically.

All images were checked for improper background subtraction (this issue was only found for F275W images in Dec. 2016) and raw values were converted to 8-bit using a constant scaling factor for each filter. Scaled images were then navigated for planet center and limb edges using an iterative ellipsoid fit. Next, reflectance (*I/F*) scale factors were computed for each image by multiplying images counts/s by the Hubble pipeline-provided radiance conversion keyword (PHOTFLAM, detector/filter inverse sensitivity in ergs/cm^2/Å/e$^-$) from the pipeline, dividing by the pixel solid angle and by the range-corrected solar flux over the detector-plus-filter band passes (see Simon et al. 2015b and Wong et al. 2020 for more processing details).

3. Zonal Trends

For our zonal analyses, singular images were chosen from the available filters for each year in Table 1, spanning the broadest possible range of dates and avoiding images where the GRS, a transiting moon, or another major feature was near the central meridian longitude (CML), Figures 1-4. Over the 2009 to 2024 period, the subsolar latitude varied between ±3.1° and the subsolar phase angle ranged from 0° to 11.4°. Because the changing

incidence and emission angles can affect the measured brightness, scans were conducted after applying a Minnaert correction of 0.52, 0.85, 0.999, and 1.0 to the F275W, F395N, F631N, and FQ889N images, respectively, derived from empirical center-to-limb fits for each filter (Simon et al. 2015). Meridional scans were made at the CML ±2.5°, collecting 500 points from -60 to +60° planetographic latitude. However, in the F395N filter, the only data available before 2014 were acquired in 2010, and there was saturation at some latitudes on the CML, see Fig. 2. To adjust for this, the meridional scan longitude on this date was shifted east of the CML by 23°. From each scan, the data were averaged over ±1° of latitude and binned every 1° to average over any small convective features and to provide several samples over each zonal wind region.

Lomb-Scargle periodograms were run across each latitude over the full available time span in each filter using the IDL scargle function (Scargle 1982). The power spectra were calculated and evaluated against false-alarm probabilities (FAP) of 10%, 5% and 1%, as seen in Fig. 5-8, right panels. The FAP is a limited measure of the true confidence level, particularly for sparsely-sampled data at long periods, but is at least instructive for identifying trends (Scargle 1982). In all filters there is evidence of long timescale changes at very low latitudes, within a few degrees of the equator. All the filters also showed evidence of a 4 to 4.5-year period near 24° N latitudes, albeit more weakly in the F275W and F631N filters. Several filters also show evidence of a 4- to 5- or 8- to 10-year periodicity near 15° to 20° N. Southern latitudes are more complicated to interpret because of large anticyclones, such as the GRS (~18° to 28° S), Oval BA (~30° to 36° S), and others near 40° S, as well as the inventing cyclonic cells; any periods below 15° S are further confounded by these large cloud features, so we do not attempt to analyze these latitudes for periodicities.

4. Longitudinal Variations

Although we avoided major storm features in choosing the images for the CML meridional scans, some latitudes still show significant longitudinal brightness variation due to storm outbreaks, general convection, and vortices. With yearly global OPAL maps, it is possible to study how longitudinal variation might affect the zonal means presented in

Section 3. For example, full longitude OPAL maps spanning ±40° of latitude are shown for several dates in each filter in Figures 9-12; these dates were chosen to span the largest brightness variations at these latitudes for comparing the cloud morphology and brightness.

Using the 9 years of OPAL maps, we analyzed the brightness for each date across 360° of longitude, finding the mean and standard deviation over ±1° of latitude, centered every 1°, as done in the periodogram analyses. Figure 13 plots these values for the latitudes of interest in each filter: 24° N (the highest velocity wind jet location along the North Temperate Belt, NTB), 14° N (the nominal NEB), 19° N (the NTrZ or expanded NEB), and 4° S or 2° N (the equatorial zone, EZ). Although these maps were not recalibrated and can have limb projection effects, temporal variations smaller than the standard deviations are less likely to indicate real periodicities. To test the robustness of our zonal analyses, and their sensitivity to longitudinal variation, we reran the periodograms from the F395N scans multiple times, allowing each scan to randomly vary by up to ± 0.1 *I/F*, about twice the measured standard deviation in Figure 13. This resulted in no change to the retrieved significant periods, lending confidence that the results are reliable.

Examining the latitudes in Figure 13, in the F275W (panel A) and FQ889N (panel D) filters, which are particularly sensitive to upper-tropospheric haze, the 24° N variations are apparent in the means. The two filters are largely anticorrelated, with the largest deviations related to superstorm outbreaks in 2016 (Sánchez-Lavega et al. 2017) and in 2020 (Figs. 9–12), preceding the OPAL observations and continuing through 2021. At 19° N variations in the UV are also apparent, at a higher frequency than at 24° N, but without an inverted signal in F889N at this latitude. These filters show little variation with longitude (small standard deviations), with one exception in the 2020 OPAL observation. Figures 9 and 12 show that the anomalously high standard deviation in 2020 was due to an isolated diffuse region of reduced haze opacity. In the NEB, at 14° N, the F395N filter, unsurprisingly, show the best evidence for an expansion cycle into 19° N on the order of 4 years, the power of which may have been masked in the periodogram analysis due to the relatively large longitudinal variations; hints of a periodogram peak at 8-10 years could be a harmonic of this period.

Finally, the EZ, shows a marked era of increased coloration starting in 2017, at the same time as the haze opacity increases in the UV/methane band. One last region of note is the 5-micron hotspot latitude, 7° N; these features appear as dark cloud holes in Fig. 11. While there is no identified periodicity at this latitude, the 5-micron hotspots essentially vanished in the 2021 OPAL data. Analyzing this latitude, we find that the 2021 F631N longitudinal mean reflectance was 0.73 with a variation of ±0.04, ~60% of the typical variation of ±0.07 when averaged over the other epochs in the 2015 to 2024 period.

5. The Great Red Spot

The GRS has been known to be shrinking and it displayed a deeper red color starting in the first few years of OPAL data, largely owing to more absorption at blue wavelengths (Simon et al. 2015b), Figure 14. There was a corresponding change in the F275W and FQ889N filters with the UV brightness decreasing and methane gas absorption band brightness increasing; this was interpreted as vertical stretching to higher altitudes to balance changes in vorticity (Simon et al. 2018). There has also been a small increase in interior velocities over time (Wong et al. 2021). Dramatic short-term changes in appearance do occur, however, often due to ingesting small eddies (e.g., Beebe et al. 1989, Rogers 1995, Sánchez-Lavega et al. 2021).

Looking over a longer time span, Figure 15, top panels, shows Minnaert-corrected meridional scans taken across the GRS center and averaged over +/-0.5° of latitude in the F275W, F395N, FQ889N filters. In all three filters, the GRS displays variability in brightness, particularly in the core, with the substantial changes already noted in the mid 2010s (Simon et al. 2015b). The average value for two locations, one in the core and one in the higher velocity collar, were plotted against time, Fig. 15 bottom panels. Despite large changes in the early dates, neither location shows a continued monotonic brightness trend in any filter over the longer time interval. The core is darker than the collar in F395N and F275W, but brighter than the collar in F889N. In each filter, changes in both the core and collar appear to be correlated over time. The temporal variation in F275W and F889N are generally anticorrelated.

6. Oval BA

Situated near 33°S latitude, three large anticyclonic ovals formed in 1939 and remained typically very pale or white in appearance (Peek 1958). Oval BA formed from the merger of those three anticyclones in the late 1990s (Sánchez-Lavega et al. 2001). Oval BA further gained notoriety in 2006 when it turned distinctly red (Simon-Miller et al. 2006, Wong et al. 2011), but its color has varied from beige to pale red since then. Figure 16 shows the changing aspect of Oval BA over time; besides color changes, it also shifts by up to 0.5° in latitude, though there is insufficient data to determine if this is a standing oscillation as is sometimes seen for large anticyclones on Jupiter and Neptune (e.g., Peek 1958, Solberg 1969, Trigo-Rodriguez et al. 2000, Sromovsky et al. 2002, Wong et al. 2018, Morales-Juberías et al. 2022).

Figure 17 shows meridional scans acquired across Oval BA, averaged in ±0.25° latitude bins owing to its much smaller size. Because the central latitude varies, the scans were shifted to center them in Fig. 17 for comparison and trending. Again, two locations were chosen, the core and the higher velocity collar. In the F275W and FQ889N filters, the core is very slightly different than the collar, but there is little variation with time. Contrary to the GRS, Oval BA's core is somewhat brighter than the collar in the F395N filter, and the color changes dramatically over time. However, variations in color seem to be again correlated across both locations. The outer edge is surrounding by a bright ring in each observation, though that ring is not as obvious when the surroundings are equally bright, such as in Fig. 16 in 2019.

7. Discussion

Periodicities, when present, are difficult to extract in sparsely sampled data, especially without many oscillation cycles, due to the inherently turbulent and chaotic nature of Jupiter's atmosphere. For example, the 2020 NEB data can be affected by the presence of a singular haze anomaly (dark in FQ889N, bright in F275W), in Figs. 9-12. On many dates convective features are visible across some longitude sections, especially in

the NEB and in the wakes of the southern anticyclones. Despite the challenges of extracting long-term trends from data containing variable compact features with significant reflectivity anomalies, some strong periods did emerge in data spanning a decade or more of coverage.

First, all of the analyzed filters show at least some evidence of a ~4- to 5-year cycle at 24° N, though it is most significant in the F395N and FQ889N filters (Figures 6 & 8). The 24° N wind jet velocity is known to be variable, with outbreaks of convective plume activity traveling with higher wind speeds, and as discussed in the introduction, that event is often tied to color changes after the event (Beebe et al. 1989, Rogers 1995, Sánchez-Lavega et al 2008, 2017, Tollefson et al. 2017, Fletcher 2017, Pérez-Hoyos et al. 2020, Wong et al. 2020, Rogers and Adamoli 2021). Infrared studies of the cloud deck and aerosol opacities also find a similar period in this region (Antuñano et al. 2019, Antuñano et al. 2023). At this latitude, the changes to the cloud morphology, cloud thickness (optical depth), cloud color, and wind speeds are likely caused by rapid overturning triggered by the rapid release of convective energy at depth (Sánchez-Lavega et al. 2008, Sankar et al. 2021). The fact that the FQ889N and F275W filters, sensitive to higher altitudes, are also affected indicates that the changes extend from quite deep to very high in the atmosphere (Sánchez-Lavega et al 2008). However, detailed radiative-transfer modeling of the 2016-2017 convective event showed that at 24° N there was very little cloud change, even though latitudes on either side experienced a change in the red “chromophore” particle altitude or optical thickness (Pérez-Hoyos et al. 2020).

Our brightness trend analyses find cycles with a 3- to 5-year period (or twice that) at latitudes in the NEB and NTrZ, again in agreement with IR results (Antuñano et al. 2019, Antuñano et al. 2023), and tied to the expansion events. This cycle begins with the colored portion expanding northward and later receding, though the cycle is sometimes incomplete or rapid (Rogers 1995, Fletcher 2017, Fletcher et al. 2017a). In our temporal analysis of the region, 2020 stands out near 19° N (Figure 13), particularly in the F395N filter. Figure 18 shows strip maps of the region from 2019 through 2022. In 2019 the region from 10° to 15° N shows a typical dark NEB appearance with small convective plumes

equatorward and small cyclonic cells near 15° N. The northern NEB/NTrZ region is lighter than the southern NEB, which is typical, with an array of small cyclonic and anticyclonic vortices from 15° to 20° N. An NEB expansion was underway in 2020, with dark coloration in both the northern and southern parts of the NEB (Rogers and Adamoli 2021). Most of the NEB then rapidly faded to a very pale appearance in 2021; the cyclonic storms are very visible as darker ovals. In the narrow-NEB phase in 2021, the typical localized convective activity in the NEB - visible as compact bright spots with trailing streamers in 2019, 2020, and 2022 - had completely shut off, only to gradually return at a single location that drifted in longitude (Rogers et al. 2022, Brueshaber et al. 2022, Wong et al. 2023). By 2022, the belt had returned to its normal appearance.

To better compare how the individual brightness variations at these latitudes correlate with observed cloud properties, we also plot the ratio of FQ889N to F275W against the ratio of F395N to F631N (Figure 19). Following Sánchez-Lavega et al. (2013), the ratio of FQ889N to F275W filters represent a measure of aerosol altitude and opacity, AOI, as they are most sensitive to the presence of the upper troposphere to lower stratosphere haze; higher or thicker aerosol layers are darker in the UV and brighter in the methane band (Sánchez-Lavega et al. 2013). At shorter wavelengths, Jupiter's spectrum shows a steep red slope with the largest regional color variations occurring due to variations at blue wavelengths (de Pater et al. 2010, Sánchez-Lavega et al. 2013, Simon et al. 2015b). Thus, the F395N to F631N ratio serves as a color index, CI, with lower values indicating redder regions.

Calculating CI and AOI from the calibrated scan data (Figures 5-8) on the 13 dates common between all four filters, the NEB (Figure 19a) showed very little temporal variation in either index. However, the EZ ratios started in the lower right (bluer and thinner or deeper aerosols) in 2015, progressed almost linearly towards the upper left in the early 2020s, and returned to less red hazes in 2024 (Figure 19a). These Hubble CI values indicate that the EZ reddened from 2017 to 2019, and gradually reverted from 2019 to 2023, while the color change was distinct in amateur data only from 2018 to 2022. In contrast, the NTrZ (19° N) showed very little variation in AOI, but much more scatter than the NEB in CI, with 2020

standing out as the reddest date (Figure 19b). Low CI values are consistent with NEB expansions into the NTrZ in ~2010, 2016, 2020, and 2024, agreeing with ground-based reports (Rogers 2019, Rogers and Adamoli, 2019, 2021). Lastly, the NTB wind jet latitude (24° N) shows substantial variation in both indices (Figure 19c), following a similar trend to that of the EZ but not linearly. After convective outbreaks in 2016 and 2020, the NTB aerosols became much redder and higher/thicker in ~2017 and 2021, with CI below ~0.55 and AOI above 0.25, before returning to their normal values (Figure 19c).

The key question is how these observed cloud level changes are tied to Jupiter's circulation below the cloud tops. With many more decades of data, and sophisticated modeling, several of these short period variations on Jupiter have been correlated with a combination of planetary-scale waves, sometimes anchored to deep vortices and convection. For example, the plume in 2020 (Fig. 9) is bright at UV wavelengths due to reflective cloud ice particles lofted to high altitudes, while the diffuse bright spot at 15° N, 245° W is likely due to locally depleted UV-absorbing haze (resulting in higher Rayleigh-scattering brightness). A periodic train of diffuse brightness variations seen in the April 2017 map (15°N, 240° to 340° W) is again due to variation in the haze concentration and is part of an upper tropospheric wave system seen more prominently in infrared imaging data from January 2017 through July 2018 (Giles et al. 2019).

Although the 4- to 5-year QQO period was long suspected to be caused by vertically propagating waves, cloud-level Rossby waves have been confirmed at 7° N and 7° S, Kelvin waves observed at the equator, and inertia-gravity waves are present all over the planet (e.g., Flasar and Gierasch 1986, Simon et al. 2015a, Orton et al. 2020). The QQO's stratospheric temperature variations peak at 13° N and S, but the effect extends to about 20° N and S (Orton et al. 1994, Cosentino et al. 2017). General circulation models of the QQO response best match observations with a forced wind jet FWHM of 8° and gravity wave drag FWHM of 5° (Cosentino et al. 2017). In other words, the dynamical effects are largely limited to the equatorial region, though the jet descends at a rate corresponding to a similar 5- to 10-year lag in the upper troposphere (Giles et al. 2020, Antuñano et al. 2023) and we do not yet know if the QQO is related to the other changes observed at the equator.

However, another potential forcing mechanism comes from Jupiter's magnetic field exciting magnetohydrodynamic waves deep in the interior Hori et al (2023). Modelling the field and wind jets, the authors find two modes that intersect with very specific half periods of 3.2 to 4.7 years at 14° to 23° N latitude, consistent with the variations we observe.

The long timescale variation seen at the equator in most filters is dominated by the obvious brightness changes that occurred from ~2018 to 2023 and noted in the OPAL data from 2015-2020 (e.g., Fry and Sromovsky 2023). Studies of infrared data also show 3.5- to 4-year, 6- to 8-year, and seasonal timescales for aerosol opacity and cloud variability at the equator (Antuñano et al. 2018, 2019, 2023). The historical record also indicates that the visible wavelength manifestation of this cycle is sometimes seasonal and sometimes not (Rogers 1995). On a seasonal scale, changing insolation might be expected to affect upper haze production, but the weak signal we find in the F275W filter, and only near the equator, does not appear to support that hypothesis, and we do not yet have enough data to conclusively see seasonal cycles. Additionally, prior radiative transfer study with a 3 -layer model, did not find that brightness changes were associated with the stratospheric layer, but rather deeper layers (Fry and Sromovsky 2023). Though the historical record is equally ambiguous on the presence of any seasonal cycles, the WFC3 data analyzed here barely cover a full Jovian year; additional years of data would also help to distinguish between cyclic and chaotic variability. It is also quite possible that several of these wave-driven mechanisms constructively and destructively interfere which is why the pattern is not predictable.

The only other evidence of a potential seasonal response is seen in the FQ889N filter at mid-northern latitudes. This is consistent with upper troposphere/stratosphere brightness temperature variations, though we find less evidence for an effect at the cloud deck (Antuñano et al. 2023). While the cause for upper tropospheric variation is unclear, seasonal effects may play a partial role. Jupiter receives only small changes in solar insolation over a Jovian year, caused more by its eccentric orbit than by its axial tilt. Because of the eccentricity, the effect is asymmetric and the largest amplitude insolation variations are seen at ~30° to 40° N latitude, though there is still some seasonal change at

all latitudes (c.f., Fig. 15 of Simon et al. (2022) and others). Additionally, although not examined here, long-period changes in Jupiter's polar hoods have been noted in the past, though primarily at UV wavelengths (Vincent et al. 2000).

Beyond the zonal cycles, we noted much more rapid changes in the appearance of Jupiter's large southern hemisphere anticyclones. The GRS showed a dramatic jump in F395N brightness in 2021 before reverting to the more usual coloration in the next data set. Oval BA changes even more rapidly from year to year. While Oval BA gets nudged southward by passing the GRS approximately every two years, it does not seem to be affected by this bump (Sánchez-Lavega et al. 2013). There does not appear to be any correlation in Oval BA's color/size/latitude to GRS passages evident in our data. Because other oscillations tend to occur on 85- to 140-day cycles for large anticyclones on Jupiter and Neptune (e.g., Peek 1958, Smith et al. 1989, Morales-Juberías et al. 2022), more frequent data are needed to discern any patterns of color tied to such behavior (Simon et al. 2024).

We do note that Oval BA sometimes appears to have a smaller footprint in the UV/methane bands most sensitive to the highest altitude clouds and hazes than in the troposphere cloud-sensitive continuum bands, Fig. 16. In the thermal infrared, de Pater et al. (2010) observed persistent 5-micron bright rings around the periphery of small Jovian anticyclones, which they argued was caused by subsidence surrounding the centrally upwelling vortex. Infrared-bright peripheral rings around the GRS and Oval BA have since been recognized to appear sporadically and sometimes incompletely (Bjoraker et al. 2018, Wong et al. 2020). The continuum brightness of 5-micron emission is influenced by cloud opacity spanning the 0.5 to 4-bar range (Bjoraker et al. 2022), while the OPAL UV/methane band data respond to the hazes above the GRS and Oval BA (and its progenitors) lying at higher altitudes, at pressures near 200 mbar (Banfield et al. 1998, Simon-Miller et al. 2001). The combined observations of sporadic 5-micron bright rings, as well as variability in the edges of the overlying haze envelopes from OPAL, may be measurable effects of variation in subsidence taking place at multiple altitude levels around the periphery of the largest anticyclones.

8. Conclusions

Long-term data sets are of vital importance for understanding changes on Jupiter. While ground based data can supplement, the calibrated photometry and UV coverage from Hubble/OPAL are irreplaceable. Using 10 years of data from OPAL, plus additional earlier WFC3 data, we have now completed a new analysis of large-scale Jupiter trends. We find clear evidence of a 4- to 5-year period at 24° N that was only hinted at in prior Hubble data. There are also suggestions of seasonal cycles, especially at the equator, but more years of data are needed to confirm. The remaining challenge is to understand why cycles are not always observed or are incomplete. It is possible that waves are always present, but just not visible in the clouds, or another mechanism can interrupt the cycles. Further circulation modeling of atmospheric wave interactions, incorporating multiple mechanisms and modes, would also be instructive in this area.

Several latitudes show interesting behavior that could benefit from more detailed radiative transfer and general circulation modeling. Most notable is the plume outbreak near 24° N that occurred in 2020. This event happened during a NEB fade/revival cycle and was accompanied by a brief episode of unusual coloration at northern mid latitudes now confirmed by these data. A detailed examination of all available calibrated data sets during that time, plus general circulation modeling, would be instructive for understanding how the events were correlated and the underlying mechanism for the color change.

Future work will study short period variations of the GRS and Oval BA, as well as a further study of longitudinal variations at latitudes of interest once a full Jupiter year of OPAL data have been acquired. As OPAL observes all 4 giant planets, analysis of the brightness periodicities for each of them would also be relevant for comparative studies of the wave and convective processes in each atmosphere. There is also a need for similar observation programs with other telescopes, such as the James Webb Space Telescope in the infrared and with future UV-visible telescopes.

Acknowledgments

This review includes observations made with the NASA/ESA Hubble Space Telescope obtained from the Space Telescope Science Institute, which is operated by the Association of Universities for Research in Astronomy, Inc. (AURA), under NASA contract NAS 5–26555. The authors were supported by a grant associated with continuing program GO13937. The individual Hubble images used in these analyses are available at: doi.org/10.17909/v0qw-x584. OPAL maps are available at: doi.org/10.17909/T9G593 (Simon 2015). The authors thank our reviewers for constructive comments that improved the manuscript and figures.

References

Antuñano, A., Fletcher, L.N., Orton, G.S., et al. 2019. *Astron. J.* 158, 130. DOI: 10.3847/1538-3881/ab2cd6.

Antuñano, A., Fletcher, L.N., Orton, G.S., et al. 2018. *Geophys. Res. Lett*. 45, 10–987. DOI: 10.1029/2018GL080382

Antuñano, A., Cosentino, R.G., Fletcher, L.N., et al. 2021. *Nature Astronomy* 5, 71–77. DOI: 10.1038/s41550-020-1165-5

Antuñano, A., Fletcher, L.N., Orton, G.S., et al. 2023. *JGR Planets* 128, e2022JE007693. DOI:10.1029/2022JE007693

Asay-Davis, X.S., Marcus, P.S., Wong, M.H., de Pater, I. 2011. *Icarus* 211, 1215-1232. DOI: 10.1016/j.icarus.2010.11.018

Baldwin, M.P., Gray, L.J., Dunkerton, D.J., et al. 2001. *Rev. Geophys*. 39, 179–230. DOI: 10.1029/1999RG000073

Banfield, D., Gierasch, P.J., Bell, M., et al. 1998. *Icarus* 135, 230–250. DOI: 10.1006/icar.1998.5985

Beebe, R.F. 1994. Jupiter: The Giant Planet. (Washington, DC: Smithsonian Institution Press).

Beebe, R.F., Orton, G.S., West, R. A. 1989. Time-Variable Nature of Jovian Cloud Properties and Thermal Structure: An Observational Perspective in Time Variable Phenomena in the Jovian System. NASA Special Publication Series, NASA-SP-494, 324-343

Bjoraker, G.L., Wong, M.H., de Pater, I., et al. 2018. *The Astronomical Journal* 156, 101. DOI: 10.3847/1538-3881/aad186

Bjoraker, G.L., Wong, M.H., de Pater, I., Hewagama, T., Ádámkovics, M. 2022. *Remote Sensing* 14, 4567. DOI: 10.3390/rs14184567

Brueshaber, S., Orton, G., Zhang, Z., et al. 2022. *European Planetary Science Congress Abstracts*, EPSC2022-733. DOI: 10.5194/epsc2022-733

Cosentino, R.G., Morales-Juberías, R., Greathouse, T., et al. 2017. *J. Geophys. Res*. 122, 2719–2744. DOI: 10.1002/2017JE005342

de Pater, I., Wong, M.H., Marcus, P.S., et al. 2010. *Icarus* 210, 742-762. DOI: 10.1016/j.icarus.2010.07.027

de Pater, I., Sault, R.J., Moeckel, C. et al. 2019. *The Astronomical Journal* 158, 139. DOI: 10.3847/1538-3881/ab3643

Flasar, F.M. and Gierasch, P.J. 1986. *J. Atmos. Sci*. 43, 2683–2707. DOI:10.1175/1520-0469(1986)043<2683:MWAAPO>2.0.CO;2

Fletcher, L.N. 2017. *Geophys. Res. Letters* 44, 4725-4729. DOI: 10.1002/2017GL073806

Fletcher, L.N., Orton, G.S., Sinclair, J.A., et al. 2017a. *Geophys. Res. Lett*. 44, 7140–7148, 10.1002/2017GL073383

Fletcher, L.N., Orton, G.S.,Rogers, J.H, et al. 2017b. *Icarus* 286, 94-117, 10.1016/j.icarus.2017.01.001

Fry, P.M. and Sromovsky, L.A. 2023. *Icarus* 389, 115224. DOI: 10.1016/j.icarus.2022.115224

Giles, R.S., Greathouse, T.K., Cosentino, R.G., Orton, G.S., Lacy, J.H. 2020. *Icarus* 350, 113905. DOI :10.1016/j.icarus.2020.113905

Giles, R.S., Orton, G.S., Stephens, A.W., et al. 2019. *Geophysical Research Letters* 46, 1232–1241. DOI: 10.1029/2018GL081858

Hori, K., Jones, C., Antuñano, A., Fletcher, L., Tobias, S. 2023. *Nature Astronomy* 7, 825–835. DOI: 10.1038/s41550-023-01967-1

Johnson, P., Morales-Juberias, R., Simon, A., et al. 2018. *Planetary and Space Sci.* 155, 2-11. DOI: 10.1016/j.pss.2018.01.004

Karkoschka, E., Koekemoer, A.M. 2003. In *Proc. 2002 HST Calibration Workshop*, ed. S. Arribas, A. Koekemoer, B. Whitmore (Baltimore, MD: STScI), 315

Legaretta, J., Barrado-Izagirre, N., Garcia-Melendo, E., et al. 2016. *Astron. & Astrophy*. 586, A154. DOI: 10.1051/0004-6361/201526197

Leovy, C.B., Friedson, A.J., Orton, G.S. 1991. Nature 354, 380–382. DOI: 10.1038/354380a0

Marinelli, M. and Dressel, L. 2024. *Wide Field Camera 3 Instrument Handbook, Version 16*. (Baltimore, MD: STScI)

McMaster, M. Biretta, J, Baggett, S. et al. 2008. *Wide Field and Planetary Camera 2 Instrument Handbook, version 10*. (Baltimore, MD: STScI).

Morales-Juberías, R., Simon, A.A., Cosentino, R.G. 2022. *Icarus* 372, 114732. DOI: 10.1016/j.icarus.2021.114732

Orton, G.S., Friedson, A.J., Baines, K.H., et al. 1991. *Science* 252, 537–542. DOI: 10.1126/science.252.5005.537

Orton, G.S., Friedson, A.J., Yanamandra-Fisher, P.A., et al. 1994. *Science* 265, 625-631. DOI:10.1126/science.265.5172.625

Orton, G.S., Tabataba-Vakili, F., Eichstädt, G. et al. 2020. *JGR-Planets* 125, e2019JE006369. DOI: 10.1029/2019JE006369

Pérez-Hoyos, S., Sánchez-Lavega, A., Sanz-Requena, J.F., et al. 2020. *Icarus* 352, 114031. DOI: 10.1016/j.icarus.2020.114031

Rogers, J.H. 1995. The Giant Planet Jupiter. (Cambridge, UK: Cambridge University Press)

528 Rogers, J., Adamoli, G., Hahn, G., et al. 2013. *European Planetary Science Congress*,
529 Abstract EPSC2013-384
530 (https://meetingorganizer.copernicus.org/EPSC2013/EPSC2013-384.pdf)

531 Rogers, J.H. 2019. Jupiter's North Equatorial Belt and Jet: I. Cyclic expansions and
532 planetary waves. *J. Brit. Astron. Assoc*. 129, 13-26. http://arxiv.org/abs/1707.03343

533 Rogers, J.H. & Adamoli, G. 2019. Jupiter's North Equatorial Belt and Jet: III. The 'great
534 northern upheaval' in 2012. *J. Brit. Astron. Assoc*. 129, 158-169.
535 http://arxiv.org/abs/1809.09736

536 Rogers, J. & Adamoli, G. 2021. Jupiter in 2020, Report no.9: Final report on northern
537 hemisphere. https://britastro.org/section_information_/jupiter-section-
538 overview/jupiter-in-2020/jupiter-in-2020-report-no-9-final-report-on-northern-
539 hemisphere

540 Rogers, J., Mizumoto, S., Hansen, C., et al., 2022. *European Planetary Science Congress*
541 *Abstracts*, EPSC2022-17. DOI: 10.5194/epsc2022-17

542 Sánchez-Lavega, A., Orton, G.S., Morales, R., et al. 2001. *Icarus* 149, 491-495. DOI:
543 10.1006/icar.2000.6548

544 Sánchez-Lavega, A., Orton, G.S., Hueso, R., et al. 2008. *Nature* 451, 437. DOI:
545 10.1038/nature06533

546 Sánchez-Lavega, A., Legarreta, J., Garcia-Melendo, E., et al. 2013. *JGR-Planets* 118, 1-21,
547 DOI: 10.1002/2013JE004371

548 Sánchez-Lavega, A., Rogers, J.H., Orton, G.S., et al., 2017, *Geophysical Research Letters*
549 44, 4679–4686 DOI: 10.1002/2017GL073421

550 Sánchez-Lavega, A., Anguiano-Arteaga, A., Iñurrigarro, P., et al. 2021 *JGR-Planets* 126, 1
551 e06686, DOI: 10.1029/2020JE006686

552 Sankar, R., Klare, C., Palotai, C. 2021. *Icarus* 368, 114589 DOI:
553 10.1016/j.icarus.2021.114589

Scargle, J.D. 1982. *ApJ* 263, 835-853. DOI: 10.1086/160554

Simon, A. 2015. *Outer Planet Atmospheres Legacy ('OPAL'),* MAST Dataset https://doi.org/10.17909/T9G593.

Simon, A. A., Li, L. Reuter, D.C. 2015a. *Geophys. Res. Letters* 42, 2612-2618, DOI: 10.1002/2015GL063433

Simon, A. A., Wong, M.H., Orton, G.S. 2015b. *ApJ* 812, 55, DOI: 10.1088/0004-637X/812/1/55

Simon, A.A., Tabataba-Vakili, F., Cosentino, R., et al. 2018. *AJ* 155, 151, DOI: 10.3847/1538-3881/aaae01

Simon, A.A., Wong, M.H., Sromovsky, L A., Fletcher, L.N., Fry, P.M. 2022. *Remote Sensing* 14, 1518. DOI: 10.3390/rs14061518

Simon, A.A., Wong, M.H., Marcus, P.S., Irwin, P.J.G. 2024. *PSJ*, DOI: 10.3847/PSJ/ad71d1

Simon-Miller, A.A., Chanover, N.J., Orton, G.S., et al. 2006. *Icarus* 185, 558-562. DOI: 10.1002/2014JE004688

Simon-Miller, A.A. and Gierasch, P.J. 2010. *Icarus* 210, 258-269. DOI: 10.1016/j.icarus.2010.06.020

Simon-Miller, A.A., Banfield, D., Gierasch, P. J., 2001. *Icarus* 154, 459–474. DOI: 10.1006/icar.2001.6742

Smith, B.A., Soderblom, L.A., Banfield, D. et al. 1989. *Science* 246, 1422-1449. DOI: 10.1126/science.246.4936.1422

Solberg H. G. 1969. *Planetary and Space Science* 17, 1573–1580. DOI: 10.1016/0032-0633(69)90146-9

Sromovsky, L.A, Fry, P.M., Baines, K.H. 2002. *Icarus* 156, 16-36. DOI: 10.1006/icar.2001.6761

578 Tollefson, J., Wong, M.H., de Pater, I., et al. 2017. Changes in Jupiter's Zonal Wind Profile
579 preceding and during the Juno Mission. *Icarus* 296, 163-178. DOI:
580 10.1016/j.icarus.2017.06.007

581 Trigo-Rodriguez, J.M., Sanchez-Lávega, A., Gomez, J.M. et al. 2000. *Planetary and Space*
582 *Sci*. 48, 331-339. DOI: 10.1016/S0032-0633(00)00002-7

583 Vincent, M.B., Clarke, J.T., Ballester, G.E. et al. 2000. *Icarus* 143, 205-222. DOI:
584 10.1006/icar.1999.6233

585 Wacker, W.K. 1975. *The Strolling Astronomer (Journal of the ALPO)* 25, 145-173.

586 Wong, M.H. 2011, in *Proc. 2010 STScI Calibration Workshop*, ed. S. Deustua & C. Oliveira
587 (Baltimore, MD: STScI), 189

588 Wong, M. H. 2010, Amplitude of Fringing in WFC3/UVIS Narrowband Red Filters, Tech. Rep.
589 WFC3 ISR 2010-04 (Baltimore, MD: STScI)

590 Wong, M.H., de Pater, I., Asay-Davis, X., Marcus, P.S., Go, C.Y. 2011. *Icarus* 215, 211-225.
591 DOI: 10.1016/j.icarus.2011.06.032

592 Wong, M.H., Tollefson, J., Hsu, A.I. 2018. *AJ* 155, 117. DOI: 10.3847/1538-3881/aaa6d6

593 Wong, M.H., Simon, A.A., Tollefson, J.W., et al. 2020. *The Astrophysical Journal Supplement*
594 *Series* 247, 58 DOI: 10.3847/1538-4365/ab775f

595 Wong, M.H., Marcus, P.S., Simon, A.A., et al. 2021. *Geophysical Research Letters* 48,
596 e93982, DOI: 10.1029/2021GL093982

597 Wong, M.H., Bjoraker, G.L., Goullaud, C., et al., 2023. *Remote Sensing* 15, 702. DOI:
598 10.3390/rs15030702

599

600

601

602 Table 1. Observation Years, Filters, and Feature Coverage

Year	Filters	Zonal Scan Frames[1]	Full Longitude Coverage[2]	GRS Frames[1]	BA Frames[1]	Program IDs	Notable Activity
2009	F275W	1	N	1	-	GO11559	
	FQ889N	1	N	1	1	GO12003, GO11559, GO12045	
2010	F275W	1	N	-	-	GO12119	
	F395N	1					
	F631N	1					
	FQ889N	1					
2012	F275W	1	N	1	1	GO13067	24° N storm
2014	F395N	1	N	1	1	GO13631	
	F631N	1		1	1		
	FQ889N	1		1	-		
2015	F275W	1	Y	1	1	GO13937	
	F395N	1		1	1		
	F631N	1		1	1		
	FQ889N	1		1	1		
2016	F275W	2	Y	2	2	GO14334, GO14661	24° N storm
	F395N	2		2	2		
	F631N	2		2	1		
	FQ889N	2		2	2		
2017	F275W	1	Y	1	1	GO14756, GO14661	
	F395N	2		2	2		
	F631N	1		2	2		

	FQ889N	1		1	1		
2018	F275W	1	Y	1	1	GO15262, GO14661	Equatorial coloration
	F395N	1		1	1		
	F631N	2		1	1		
	FQ889N	1		1	1		
2019	F275W	1	Y	1	1	GO15502, GO14661	Equatorial coloration
	F395N	2		1	2		
	F631N	2		1	2		
	FQ889N	2		1	2		
2020	F275W	1	Y	1	1	GO15929, GO16074	24° N storm, equatorial coloration
	F395N	1		2	1		
	F631N	1		2	1		
	FQ889N	1		2	1		
2021	F275W	1	Y	1	1	GO16266	Equatorial coloration
	F395N	1		1	1		
	F631N	1		1	1		
	FQ889N	1		1	1		
2022	F275W	2	Y	2	1	GO16913 GO16790	Equatorial coloration
	F395N	2		2	1		
	F631N	2		2	1		
	FQ889N	2		2	1		
2023	F275W	1	N	1	-	GO16790, GO17275	
	F395N	2		1	-		
	F631N	2		2	1		
	FQ889N	2		2	1		
2024	F275W	1	Y	1	1	GO16995	
	F395N	1		1	1		
	F631N	1		1	1		

	FQ889N	1		1	1		

Notes.

1. A more detailed index of all analyzed images can be found at: doi.org/10.17909/v0qw-x584

2. OPAL maps are available at: doi.org/10.17909/T9G593

Figures

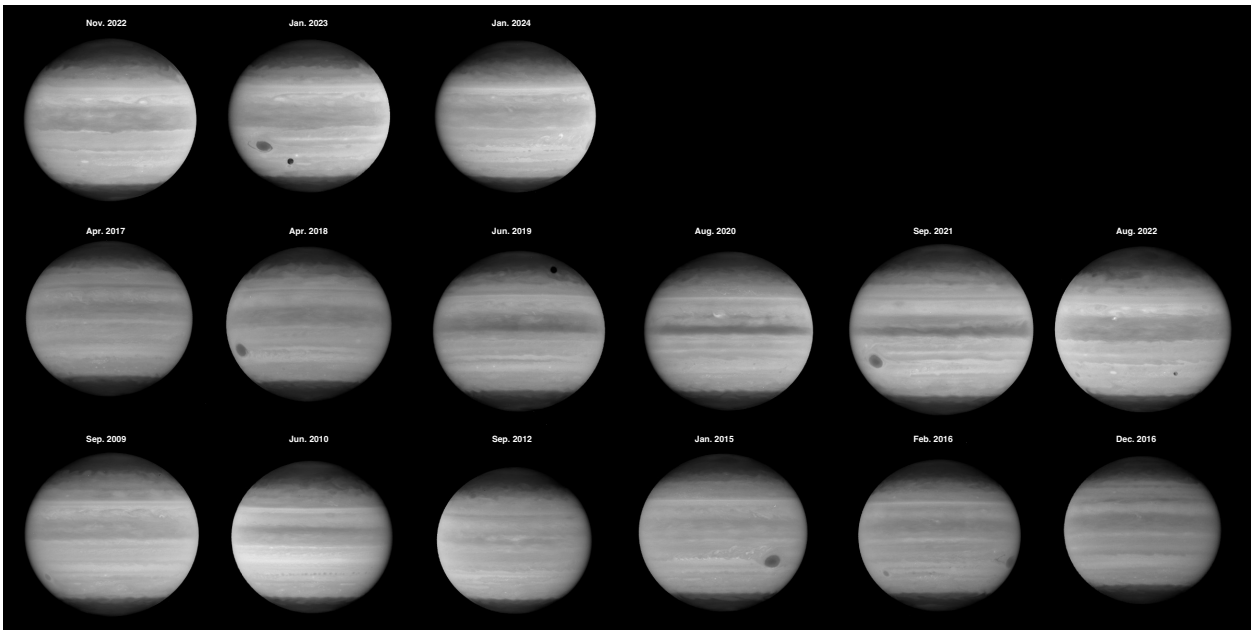

Figure 1. Images used for latitudinal scans in the F275W filter. All images are scaled over the same brightness range.

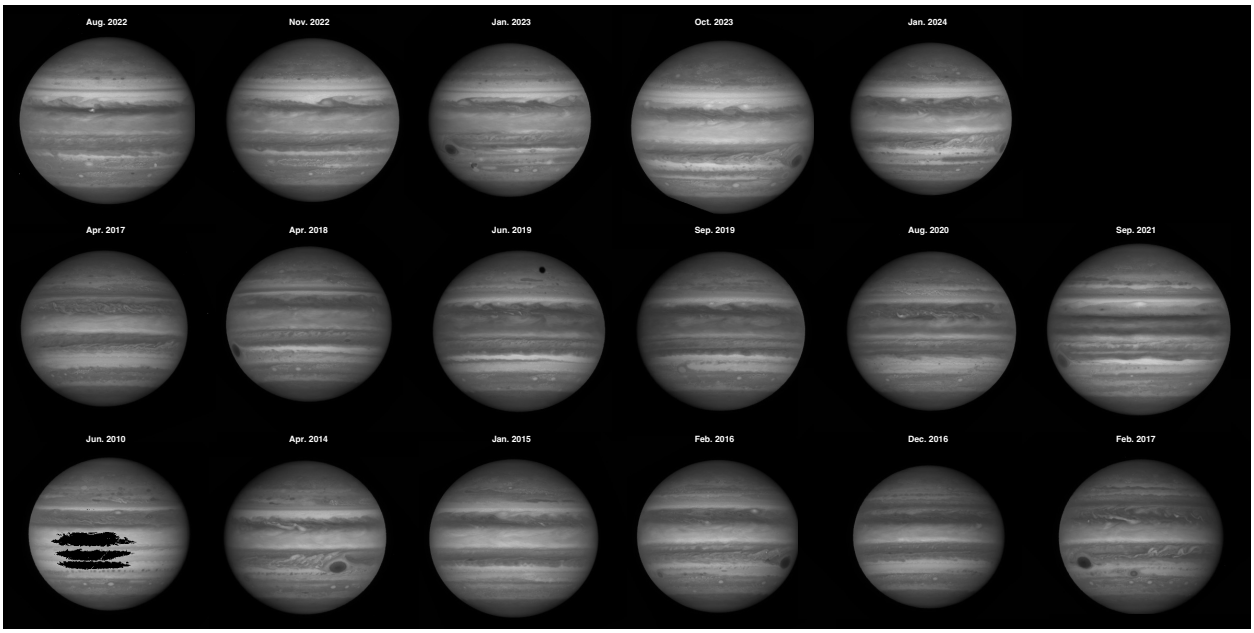

Figure 2. Images used for latitudinal scans in the F395N filter. All images are scaled over the same brightness range; the June 2010 image shows saturation near the center.

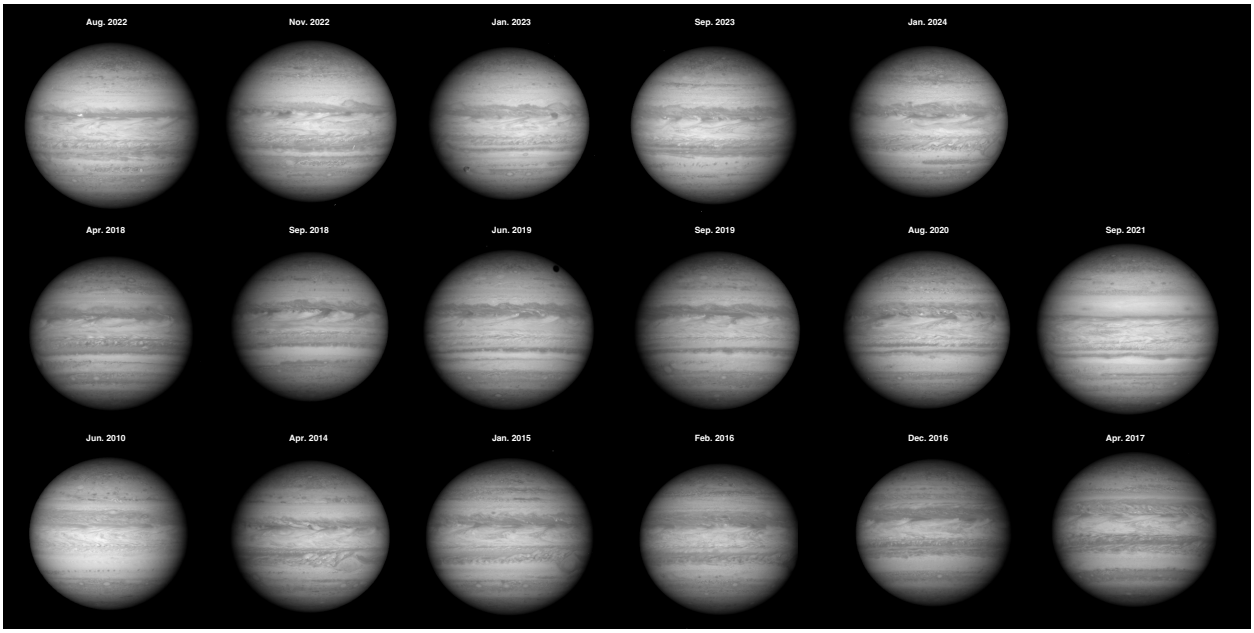

Figure 3. Images used for latitudinal scans in the F631N filter. All images are scaled over the same brightness range.

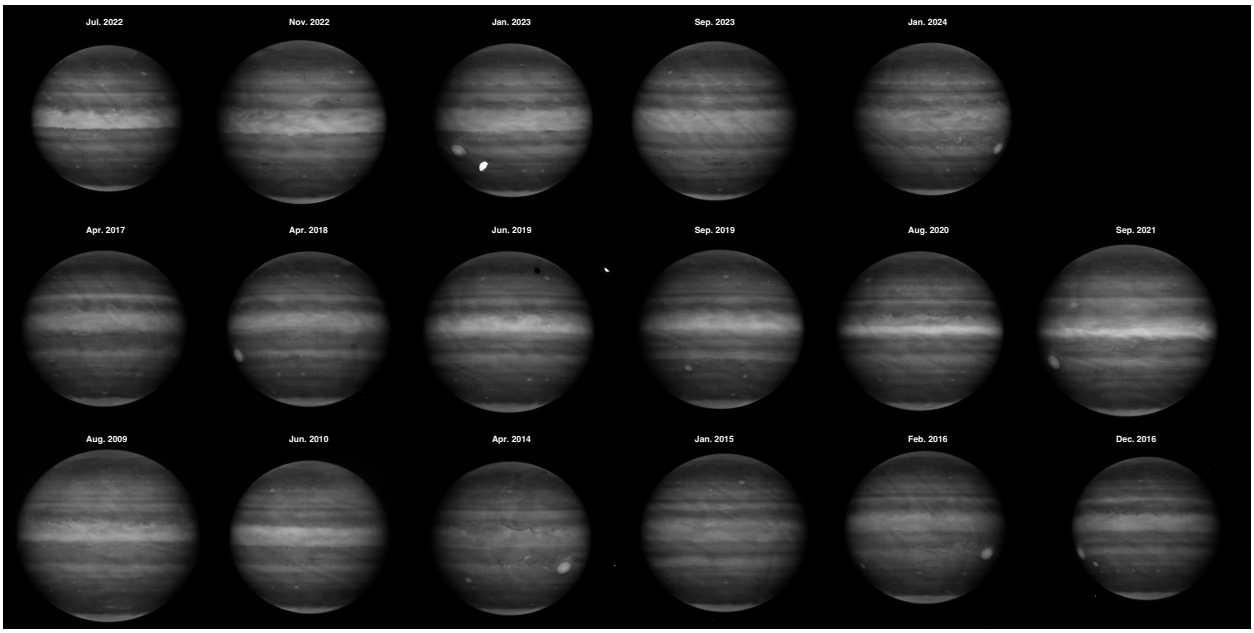

Figure 4. Images used for latitudinal scans in the FQ889N filter. All images are scaled over the same brightness range; the Jan 2023 image shows a saturated satellite transiting.

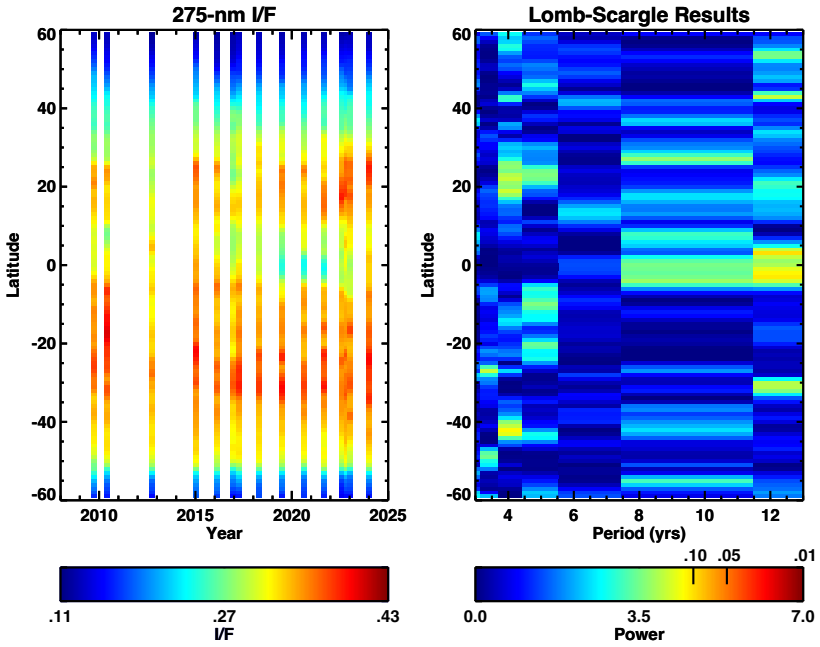

Figure 5. F275W brightness scans (left) and Lomb-Scargle periodogram (right).

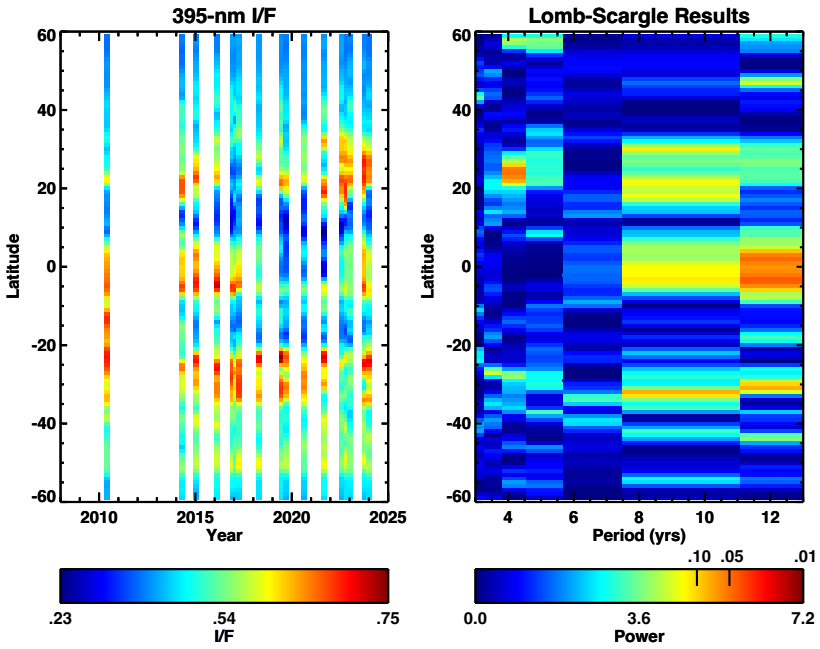

629

630 Figure 6. F395N brightness scans (left) and Lomb-Scargle periodogram (right).

631

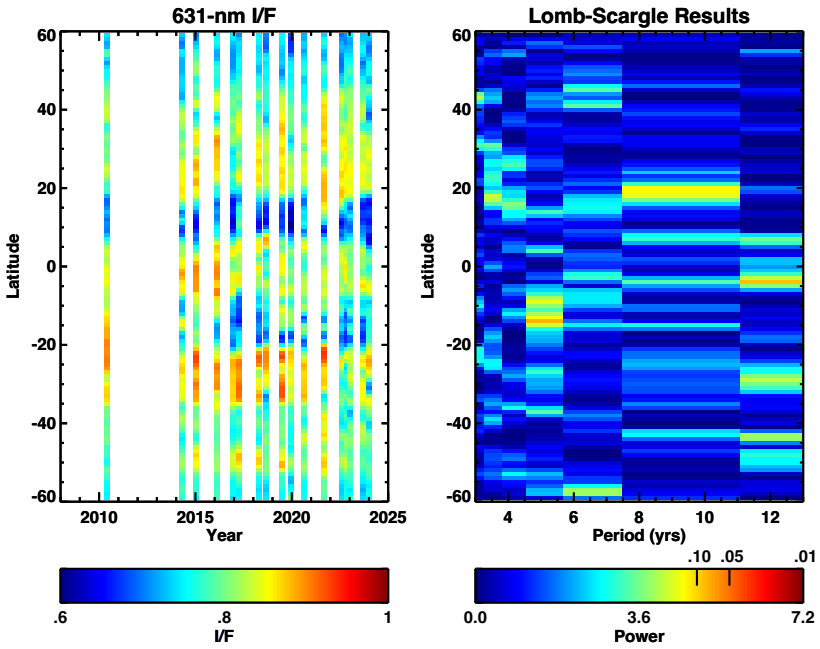

632

633 Figure 7. F631N brightness scans (left) and Lomb-Scargle periodogram (right).

634

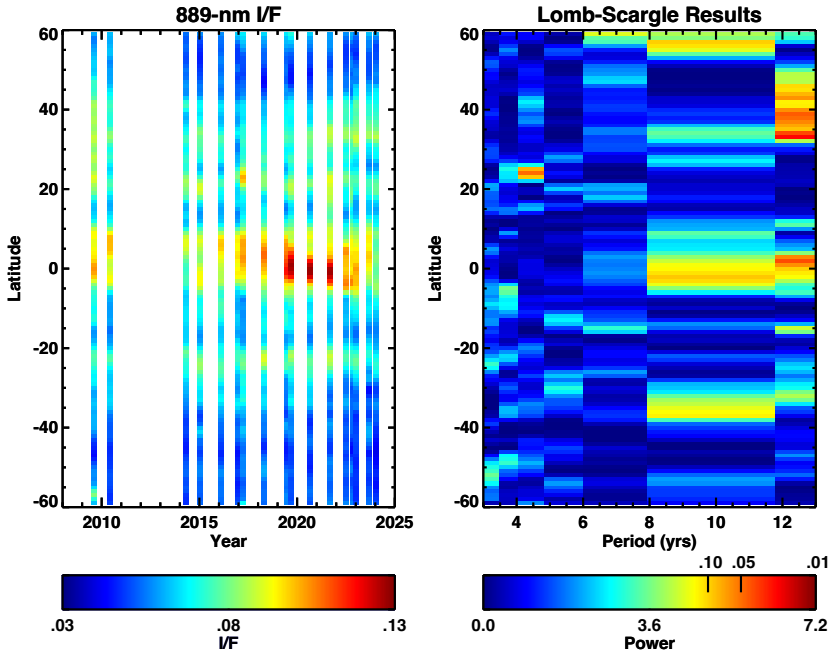

Figure 8. FQ889N brightness scans (left) and Lomb-Scargle periodogram (right).

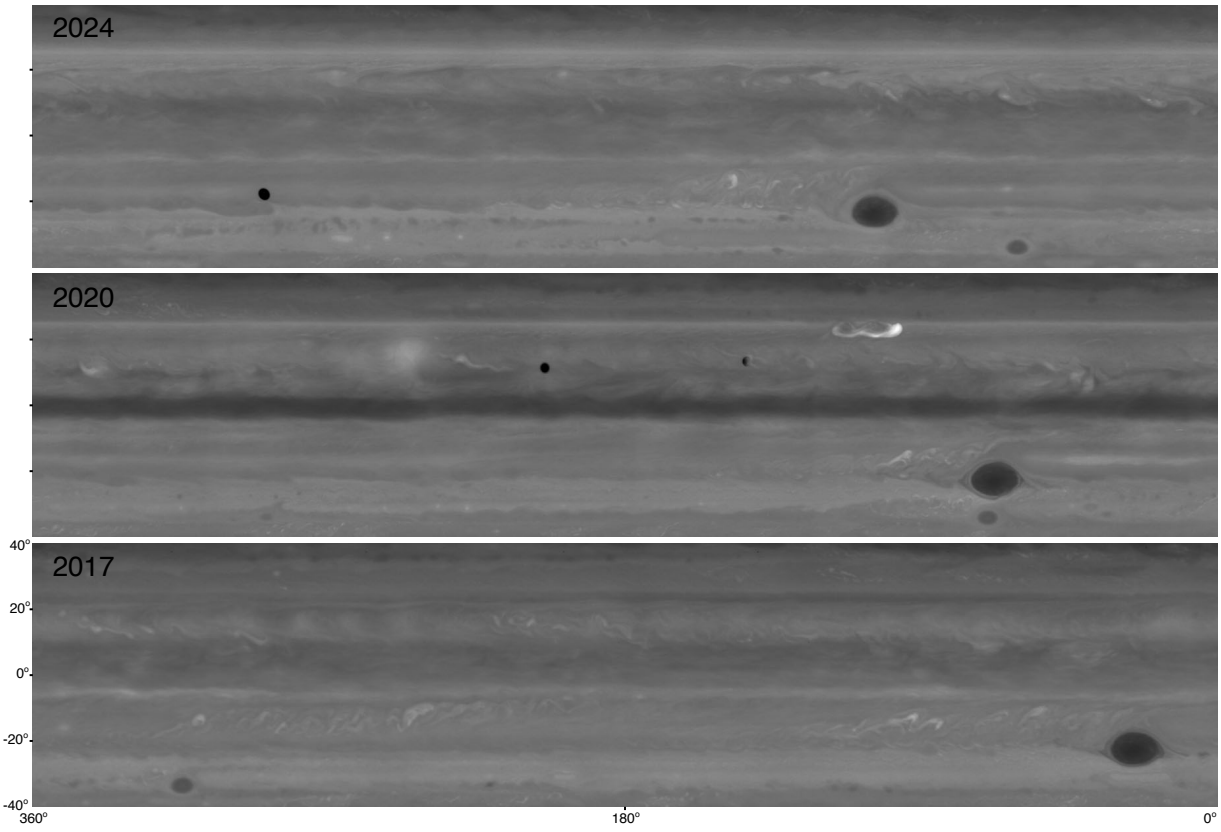

Figure 9. F275W maps covering all longitudes and +/-40° latitude for 3 dates, contrast scaled the same. A large active plume was visible in 2020 near 20° N, 100° W and a periodic train of diffuse brightness variations are visible in the April 2017 map (15° N, 240° to 340° W).

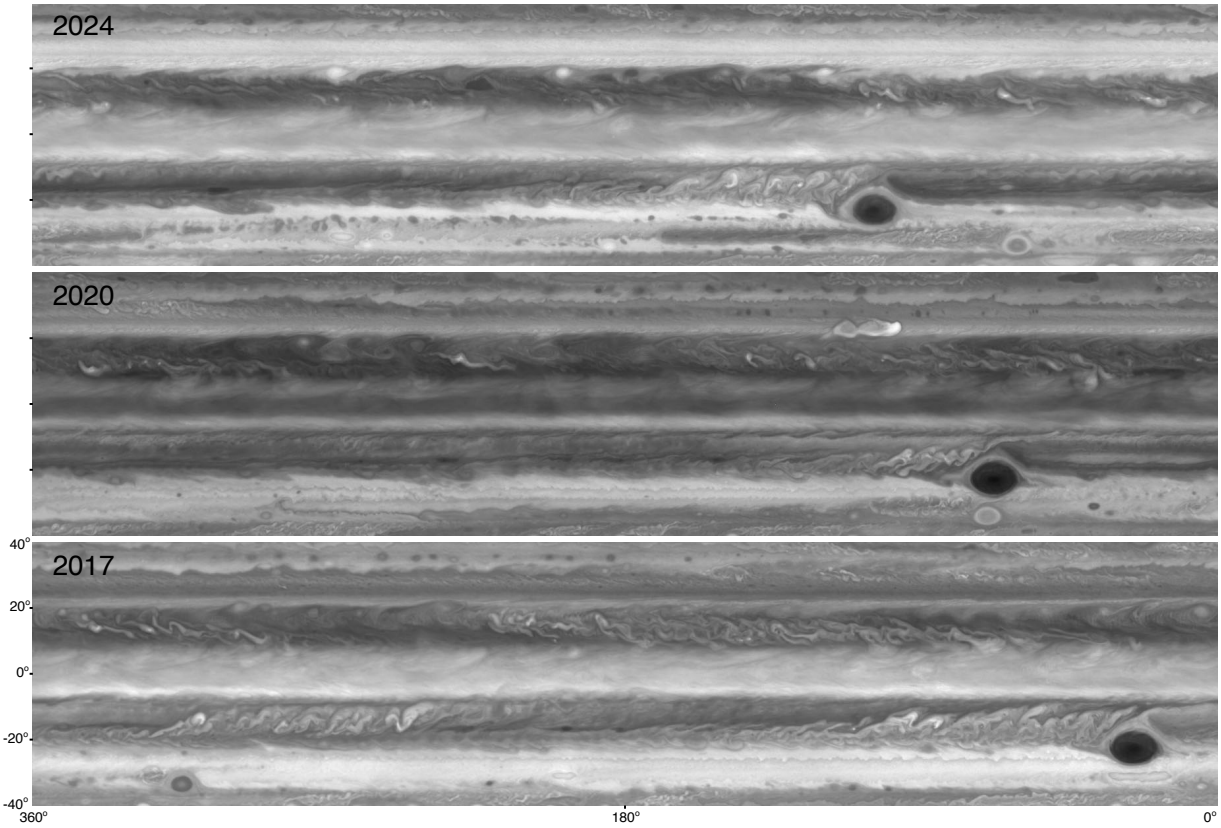

Figure 10. F395N maps covering all longitudes and +/-40° latitude for 3 dates, contrast scaled the same. Longitudinal structure varies widely with latitude and date.

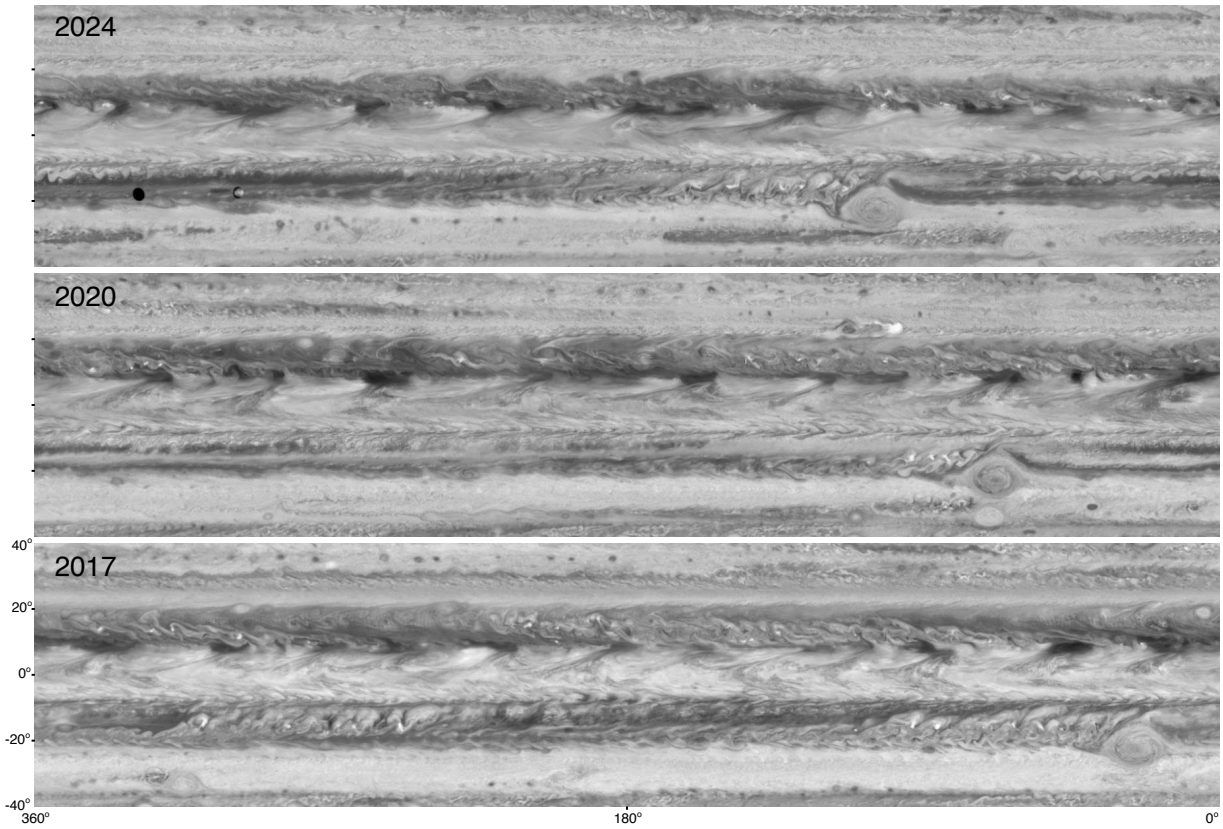

Figure 11. F631N maps covering all longitudes and +/-40° latitude for 3 dates, contrast scaled the same. Dark regions are cloud clearings, “hotspots” at edge of equatorial zone are prominent.

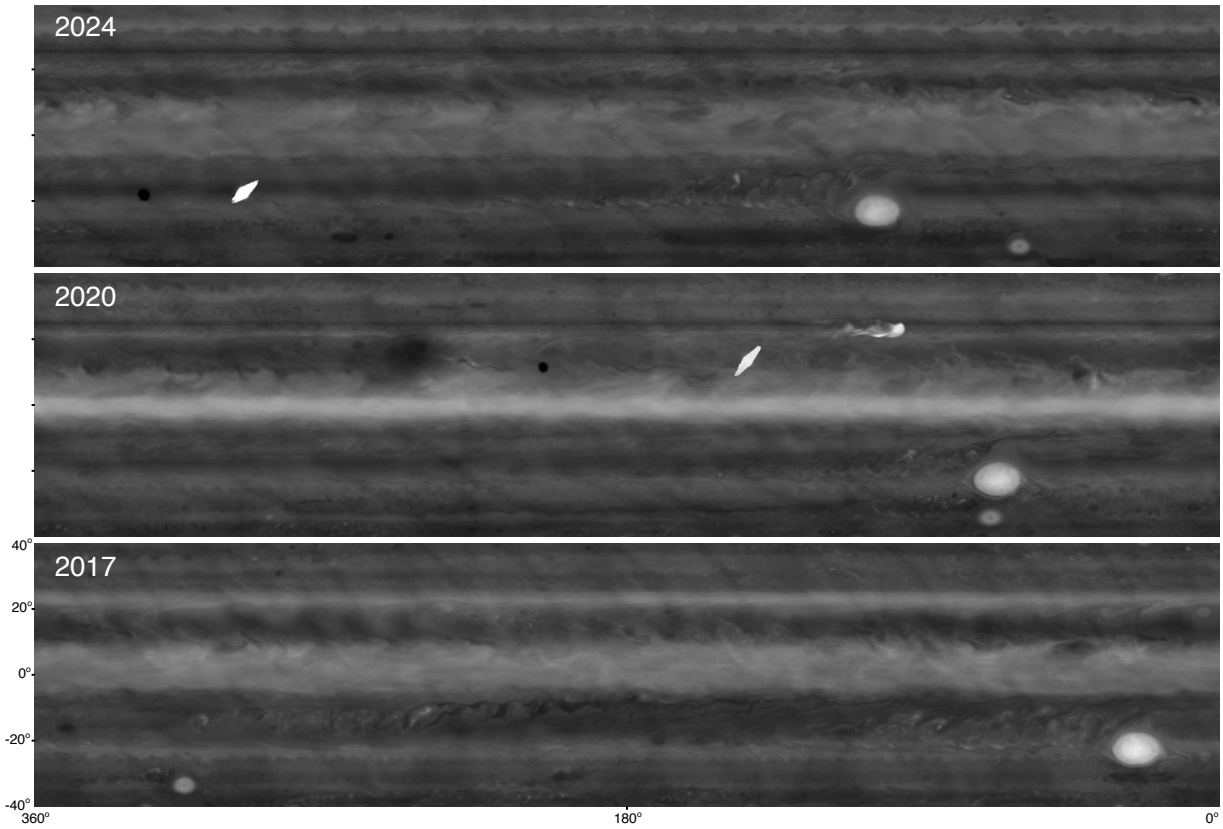

Figure 12. FQ889N maps covering all longitudes and +/-40° latitude, contrast scaled the same. Small amplitude residual fringing is apparent, and transiting moons saturate (visible in 2020 and 2024). The diffuse bright spots in the F275W data (Fig. 9, faint periodic spots in 2017 and a high-intensity, isolated, spot in 2020) appear dark in the methane-band maps.

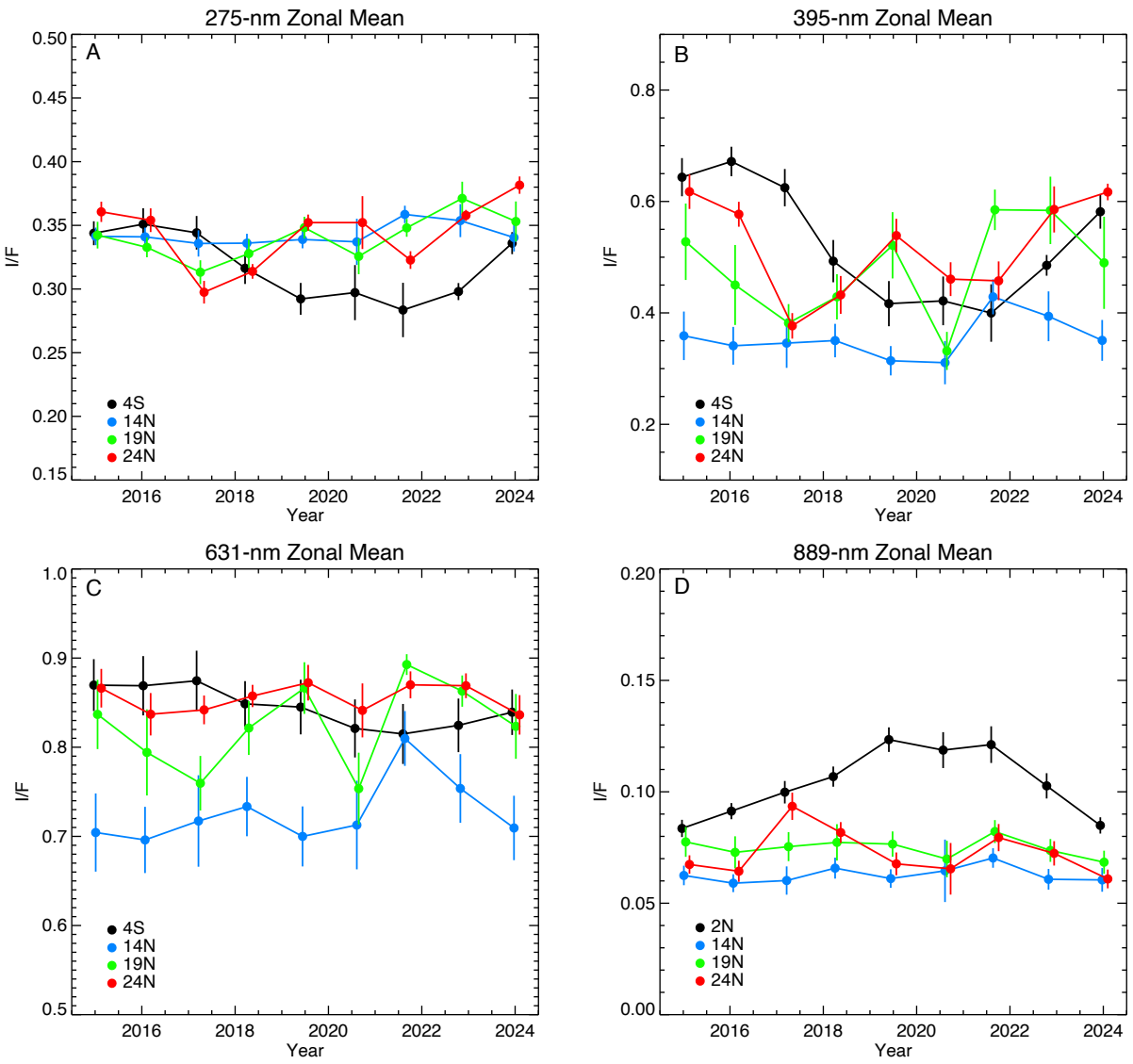

Figure 13. Zonal average reflectivity at select latitudes (i.e., power spectrum peaks in Figs. 5-8) with longitudinal brightness standard deviations as the uncertainty bars. A) F275W curves display the largest variations above the longitudinal standard deviations at the equator and NTB (24° N). B) F395N curves showing blue absorption changes at multiple latitudes. C) F631N curves showing variation, largely due to cloud opacity, is largest in the NTB and NTrZ (19° N). D) FQ889N curves showing upper troposphere/lower stratosphere clouds have the largest variations at the equator and NTB (24° N).

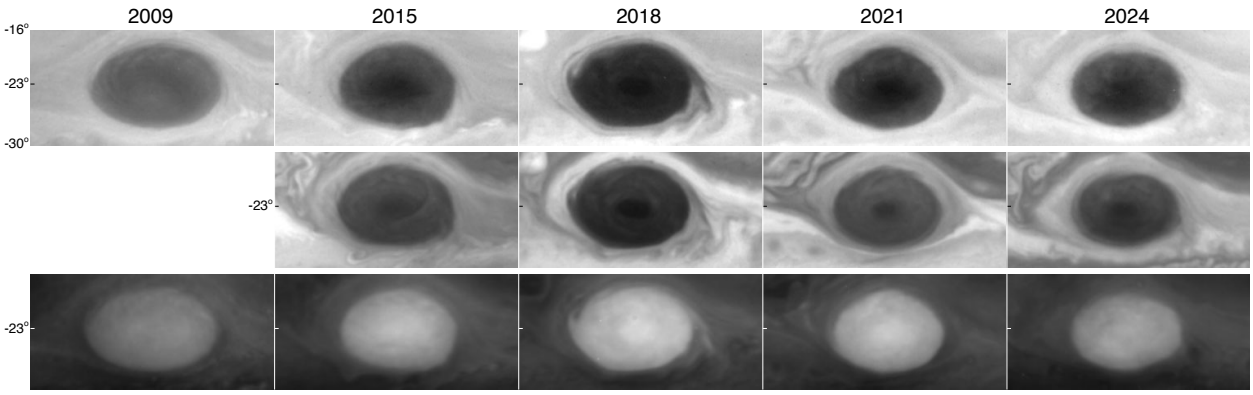

Figure 14. GRS maps centered at -23°, spanning +/- 7° latitude and +/-15° of longitude. These maps span the UV to near-IR, using the F275W (top row), F395N (middle, no data in 2009) and FQ889N (bottom) filters. In 2021, the F395N brightness temporarily increased, even though no effects were seen in the other filters.

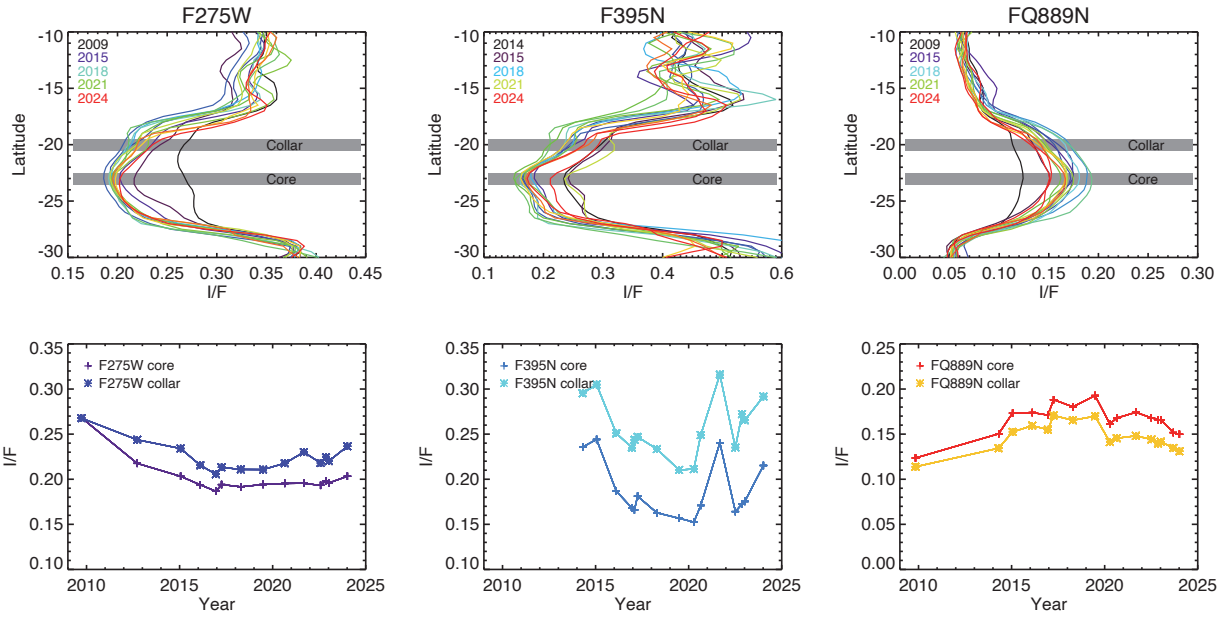

Figure 15. Brightness trends in the GRS. Meridional scans across the GRS center. Bottom: averaging over -22.5 to -23.5° to encompass the core region, and -19.5 to -20.5° for the collar.

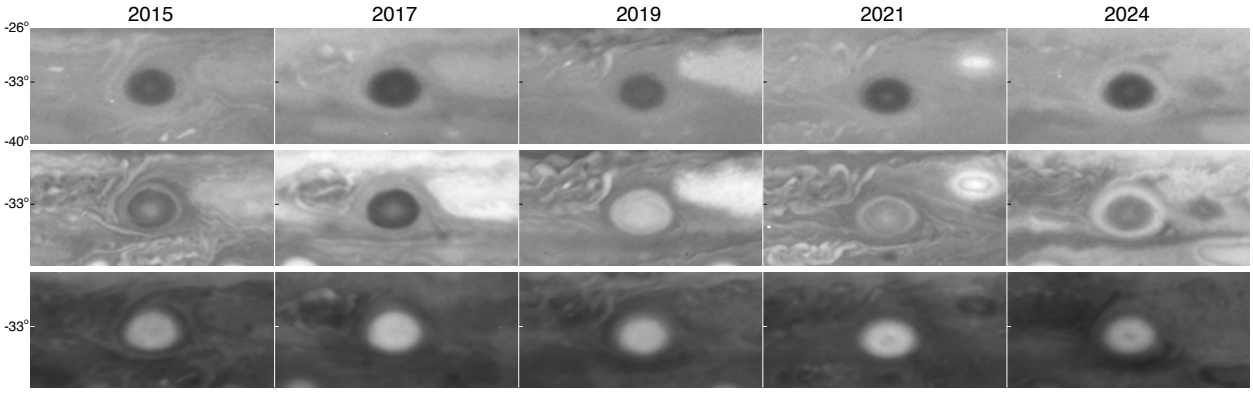

Figure 16. Oval BA maps centered at -33°, spanning +/- 7° latitude and +/-15° of longitude. These maps span the UV to near-IR, using the F275W (top), F395N (middle) and FQ889N (bottom) filters. In 2021, the F395N brightness temporarily increased, even though no effects were seen in the other filters.

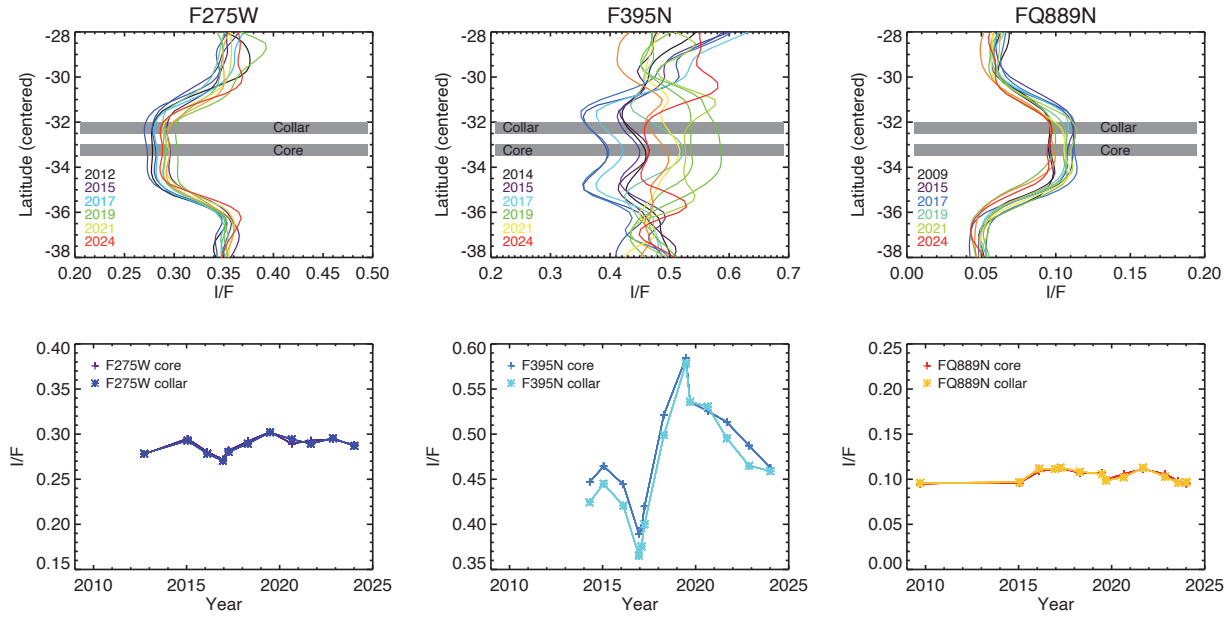

Figure 17. Brightness trends in Oval BA. Meridional scans across Oval BA center; note several dates had to be shifted to align the core region, notably 2021. Bottom: averaging over -33° to -33.5° to encompass the core region, and -32° to -32.5° for the collar.

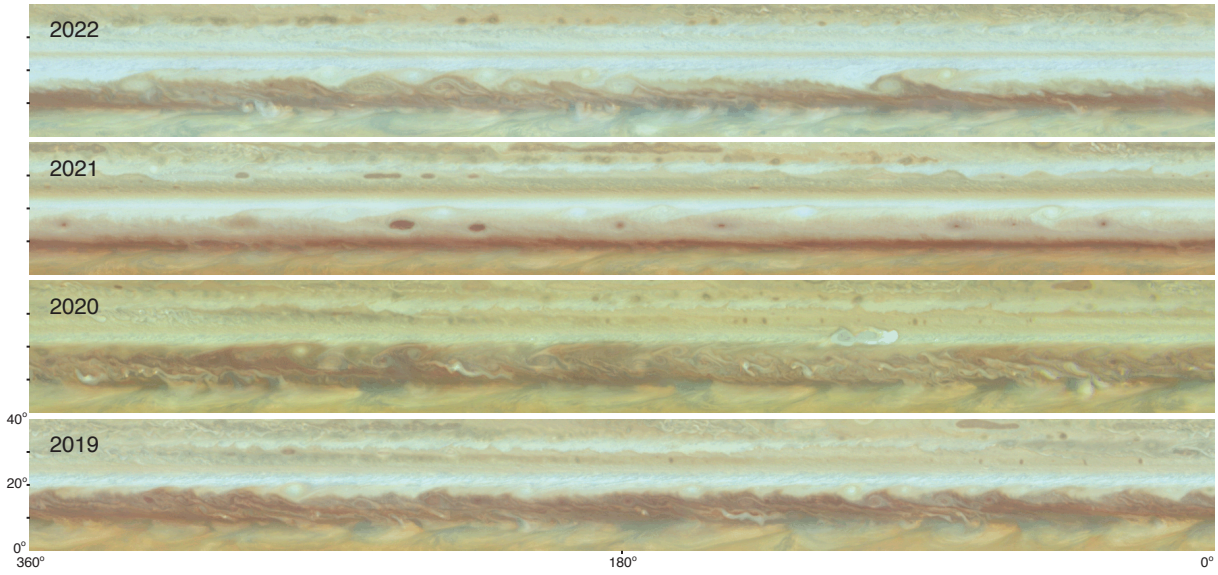

Figure 18. The North Equatorial Belt (NEB) from 2019 to 2022. These color strip maps (R: F631N, G: F502N, B: F395N, with identical scaling between dates) span a limited latitude range to highlight the rapid changes that occur in the NEB from 10° to 20° latitude. A dark appearance with convective streamers, such as 2019 and 2020, is common. In 2020, the overlying haze is darker from ~20° to 35°, perhaps due to the active plume and NEB expansion.

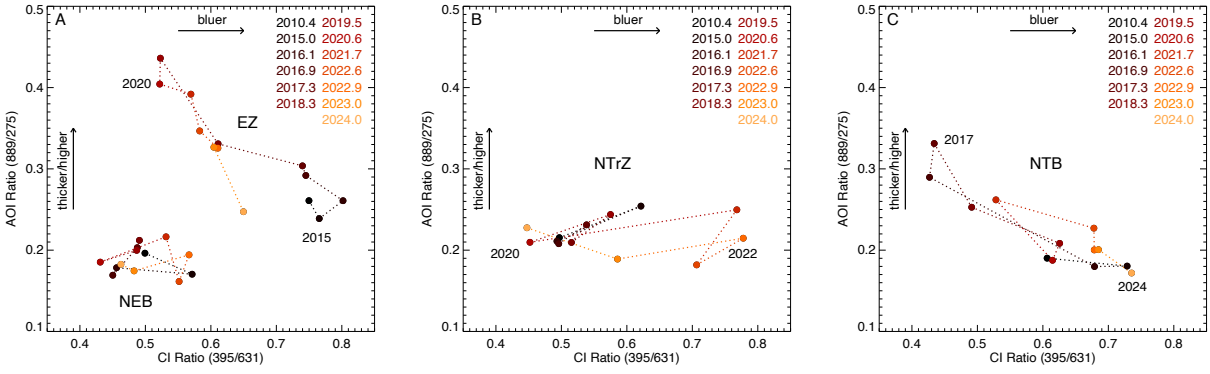

Figure 19. Altitude / opacity (AOI) and color (CI) indices for the latitudes shown in Figure 13, from the scans in Figures 5-8, using the 13 dates with observations in all four filters. A) The NEB shows limited changes primarily in CI, while the EZ changed dramatically in both over the period of this study. B) The NTrZ (19° N) mostly varies in CI, with 2020 has an outlier,

consistent with Figure 18. C) The NTB jet (24° N) varies in AOI and CI in a manner similar to the EZ, but with rapid changes occurring after convective outbreaks.